1993

Mathematical Modeling of the Formation of Calcareous Deposits on Cathodically Protected Steel in Seawater

J. F. Yan
University of South Carolina - Columbia

T. V. Nguyen
University of South Carolina - Columbia

Ralph E. White
University of South Carolina - Columbia, white@cec.sc.edu

R. B. Griffin
Texas A & M University - College Station

Publication Info

Journal of the Electrochemical Society, 1993, pages 733-744.

Publisher's link:
http://dx.doi.org/10.1149/1.2056150
DOI: 10.1149/1.2056150

Mathematical Modeling of the Formation of Calcareous Deposits on Cathodically Protected Steel in Seawater

J.-F. Yan,*,[1] T. V. Nguyen,,[2] and R. E. White****

Department of Chemical Engineering, University of South Carolina, Columbia, South Carolina 29208

R. B. Griffin

Department of Mechanical Engineering, Texas A&M University, College Station, Texas 77843-1292

ABSTRACT

A first principle mathematical model of the formation of calcareous deposits on a cathodically protected steel rotating disk electrode in seawater is presented. The model includes equations which transport phenomena, electrochemical reactions, precipitation reactions, and a homogeneous reaction involved in the formation of calcareous deposits on an electrode surface. Predicted concentration profiles show that a high concentration of OH^- ions on the electrode surface leads to the formation of calcareous deposits. The calcareous deposits contain mostly $CaCO_3$, but the initial deposits are predicted to contain more $Mg(OH)_2$ than $CaCO_3$. The predicted calcareous deposits on the electrode surface reduce the active surface area available for the electrochemical reactions, which results in a decrease in the cathodic current density. The predicted current density as a function of time during the formation of deposits agrees qualitatively with experimental data.

The main electrochemical reactions that occur during the corrosion of steel structures in seawater are the oxidation of iron

$$Fe \rightarrow Fe^{2+} + 2e^- \quad [1]$$

the reduction of oxygen

$$O_2 + 2H_2O + 4e^- \rightarrow 4\ OH- \quad [2]$$

and hydrogen evolution

$$2H_2O + 2e^- \rightarrow H_2 + 2\ OH^- \quad [3]$$

Cathodic protection (CP) has been recognized as an effective method for preventing immersed offshore structures from corroding. Under cathodic protection, the oxidation of iron is prohibited by supplying electrons to the metal structure to be protected by means of sacrificial anodes or impressed current.[1] One feature associated with marine cathodic protection is the formation of calcareous deposits on metal surfaces.[2-4]

There has been considerable effort devoted to studying the influence of physics and chemistry of seawater, cathodic protection, and surface preparation on the formation of calcareous deposits through electrochemical experiments in natural seawater[5-12] and in artificial seawater.[13-14] However, there are very few papers regarding mathematical modeling of this phenomenon.

The only mathematical model available in the literature on the formation of calcareous deposits on cathodically protected steel in seawater was given by Sadasivan in his master's thesis.[15] His one-dimensional model considered diffusion to be the only mass-transport mechanism for the components in seawater. Only OH^-, Mg^{2+}, Ca^{2+}, HCO_3^-, and CO_3^{2-} ions were considered, which are too few to describe correctly seawater chemistry.[16] Furthermore, his equations for current density were based on the Tafel equation for hydrogen evolution and the limiting current density for oxygen reduction. Both equations do not account for the effects of changes of concentration and solution potential inside the diffusion layer.

Dexter[17] developed a steady-state model to calculate the pH at a cathodically polarized metal surface in quiescent saline waters in the presence of both calcareous deposits and biofilms. His model considered the oxygen reduction as the major cathodic reaction and diffusion as the only method for oxygen transport. However, the model ignored the formation of calcareous deposits and biofilms with time.

The main objective of this study was to develop a mathematical model of the formation of calcareous deposits on cathodically protected steel structures in seawater from first principles. This model will be helpful in understanding the mechanism of the formation of calcareous deposits on cathodically protected steel surfaces and their effects on marine cathodic protection systems. The model will be capable of predicting the changes in current density and composition of the deposits with time. The final model will be used to help predict the conditions necessary for the formation and the maintenance of calcareous films on structural steels in deep ocean water. Meanwhile, the rotating disk technique was used to grow the calcareous deposits on the cathodically protected steel in ASTM substitute ocean water.

Experiments

The electrochemical cell used in this work was cylindrical in shape (diameter = 12 cm) with a volume of about 900 cm^3 in capacity and consisted of a working electrode made of the low carbon steel specimen, a platinum counterelectrode, and a saturated calomel electrode (SCE). The experiments were done potentiostatically and the rotation speed of the disk was controlled at 50 rpm. In addition, a gas distributor was used to bubble the purified air into the solution to keep dissolved oxygen and carbon dioxide saturated during the experiment. The gas distributor was placed away from the working electrode in the electrochemical cell and the air flow rate was controlled to be very small such that the hydrodynamics around the electrode surface was not distrubed during the experiment. The arrangement of the electrochemical cell is shown in Fig. 1.

The low carbon steel was machined into a rotating disk electrode (RDE) of 0.32 cm^2 in area. The electrode was ground with SiC abrasive paper from 240 through 600 grit, and polished by 5, 0.3, and 0.03 μm Al_2O_3 powder in deionized water. Then, it was cleaned with an ultrasonic cleaner in a bath of dilute acetone solution and rinsed with deionized water. The electrode was placed in an electrochemical cell containing substitute ocean water, which was prepared according to the composition given in ASTM-D1141-90.[18] The purified air was bubbled through the solution for at least 2 h before and during the entire experiment.

At the end of the experiment, the specimen was removed immediately from the solution, rinsed with deionized water, and placed in a desiccator for further surface analyses. The scanning electron microscope (SEM) was used for morphological examination (JEOL, JSM-6400 Scanning Microscope) and elemental spectra analysis (Tracor Northern Serious II) of the calcareous deposits.

*Electrochemical Society Student Member.
**Electrochemical Society Active Member.
[1] Present address: Department of Chemical Engineering, Texas A&M University, College Station, Texas 77843.
[2] Present address: AT&T Bell Laboratories, Mesquite, Texas 75149.

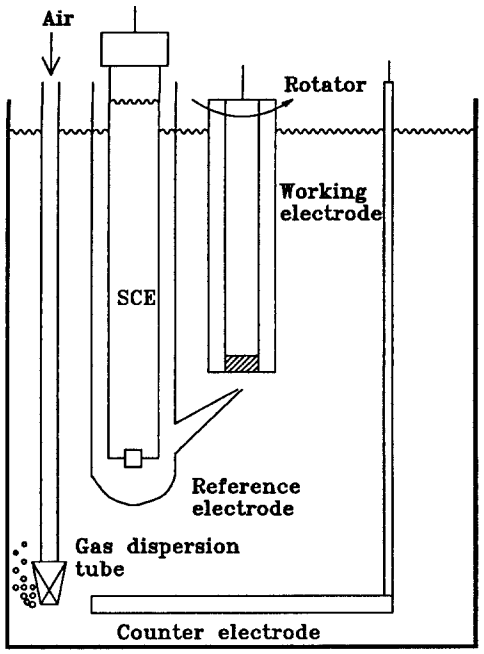

Fig. 1. Schematic of rotating disk electrode experimental cell.

Figures 2 and 3 show the calcareous deposits grown at −0.9 V (SCE) and 50 rpm after 40 and 87 h exposure, respectively. The cauliflower-like crystals, growing on the metal base, are calcareous deposits. The elemental spectra analysis from SEM-EDAX for the calcareous deposits in Fig. 3 indicates that the main constituents in the calcareous deposits are Ca, C, and O as shown in Fig. 4. Also, Mg, Sr, Na, Cl, S, and Fe are the trace elements found in the calcareous deposits. Detection of Fe might be due to the penetration of the electron beam to the underlying steel substrate. Figure 5 shows a side view of the calcareous deposit in Fig. 3. The white layer is the metal substrate. The top part shows the calcareous deposit with a thickness of about 10 μm.

Model Development

The experimental results indicate that the current density for CP decreases with time due to the formation of calcareous deposits, which is discussed further below, and our SEM pictures (see Fig. 2 and 3) show that the main change on the electrode surface is the increasing surface area covered by the calcareous deposits with no increasing thickness of the porous deposits. Therefore, the model presented in the following section is based on the fact that calcareous deposits block the active surface area available

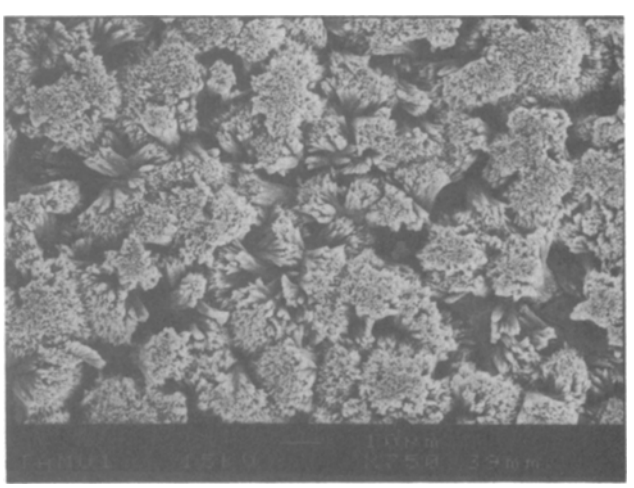

Fig. 2. Scanning electron micrograph of the calcareous deposits (top view) grown on low carbon steel rotating disk electrode in ASTM substitue ocean water at 50 rpm, −0.9 V(SCE), after 40 h.

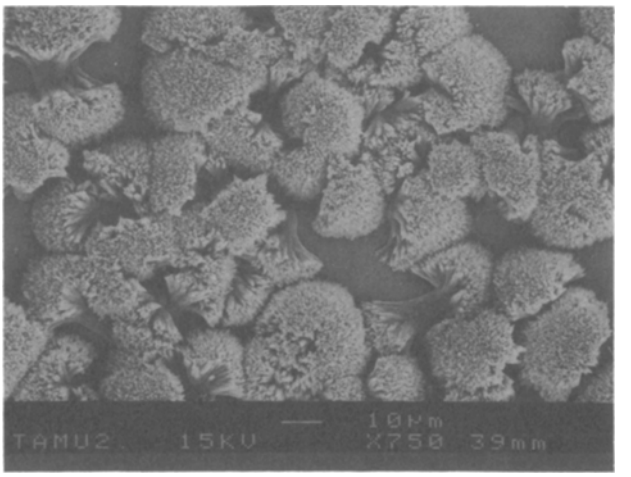

Fig. 3. Scanning electron micrograph of the calcareous deposits (top view) grown on low carbon steel rotating disk electrode in ASTM substitute ocean water at 50 rpm, −0.9 V(SCE), after 87 h.

for the electrochemical reactions and consequently reduce the current density to the disk during CP.

The proposed mechanism for the formation of calcareous deposits on cathodically protected steel in seawater is presented below. The calcareous deposits are assumed to be a mixture of $CaCO_3$ and $Mg(OH)_2$ in the model. A high concentration of OH^- ions generated by the electrochemical reactions on the electrode surface causes the precipitation of $Mg(OH)_2$

$$Mg^{2+} + 2\ OH^- \rightarrow Mg(OH)_2\downarrow \quad [4]$$

Also, the production of OH^- ions on the electrode surface changes the inorganic carbon equilibria in the adjacent seawater and facilitates the following buffering reaction[19]

$$OH^- + HCO_3^- \rightleftarrows H_2O + CO_3^{2-} \quad [5]$$

As a result, $CaCO_3$ also precipitates

$$Ca^2 + CO_3^{2-} \rightarrow CaCO_3\downarrow \quad [6]$$

Equations are presented below that are used to describe transport phenomena, electrochemical reactions, precipitation reactions, and the homogeneous reaction involved in the formation of calcareous deposits on the electrode surface. The modeled region, as shown in Fig. 6, is the diffusion layer between $y = 0$ and $y = y_{RE}$ and two boundaries at $y = 0$ and $y = y_{RE}$, which represent the electrode surface and bulk solution interfaces, respectively. It is worth noting that the thickness of the deposits, about 10 μm as shown in Fig. 5, is much less than that of the diffusion layer, 150 μm; consequently, the diffusion layer equations are used everywhere except at $y = 0$ and $y = y_{RE}$.

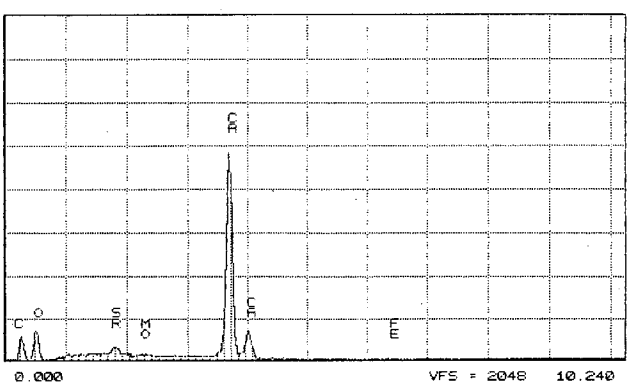

Fig. 4. Scanning electron elemental spectra of the calcareous deposits (top layer) grown on low carbon steel rotating disk electrode in ASTM substitute ocean water at 50 rpm, −0.9 V(SCE), after 87 h.

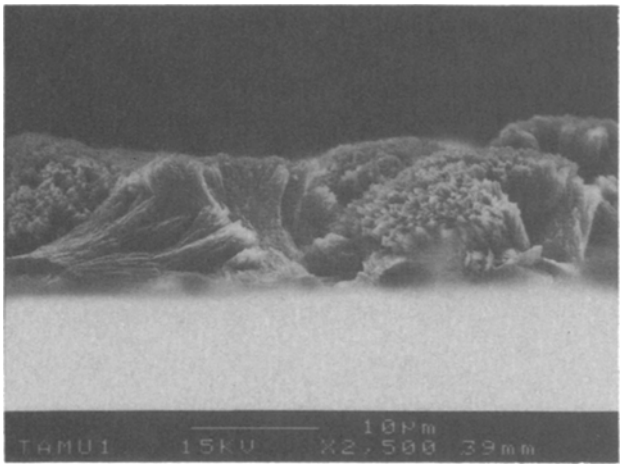

Fig. 5. Scanning electron micrograph of the calcareous deposits (side view) grown on low carbon steel rotating disk electrode in ASTM substitute ocean water at 50 rpm, −0.9 V(SCE), after 87 h.

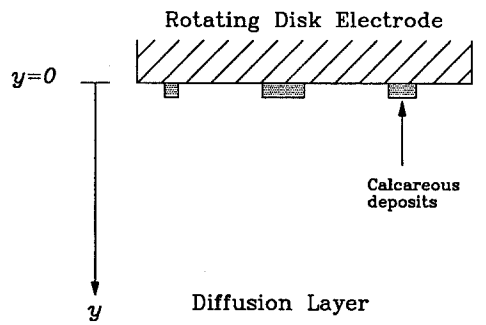

Fig. 6. Schematic of the electrode surface and the diffusion layer on a rotating disk electrode.

Before presenting the model equations, the following assumptions are made.

1. The electrolyte is isothermal.
2. Dilute solution theory is applied.
3. Double-layer charging is neglected.
4. Electrochemical reactions occur only on the uncoated surface (*i.e.*, the uncovered surface and the clean surface on the covered surface).
5. The reaction of iron, Eq. 1 can be neglected as long as the steel is under cathodic protection.
6. The precipitation reactions occur only on the uncovered surface.
7. The homogeneous reaction occurs in solution region.
8. Calcareous deposits are assumed to be a mixture of $CaCO_3$ and $Mg(OH)_2$. Also, they are assumed to be porous with constant porosity and thickness.
9. Deposits do not dissolve once they precipitate on the metal surface.
10. The nucleation process is neglected.

Some parameters used in the model are defined as follows. Surface coverage θ (see Fig. 7) is defined as the ratio of total surface area covered by porous deposits (A_s) to the total electrode surface area (A_o)

$$\theta = \frac{\Sigma A_i}{A_o} = \frac{A_s}{A_o} \qquad [7]$$

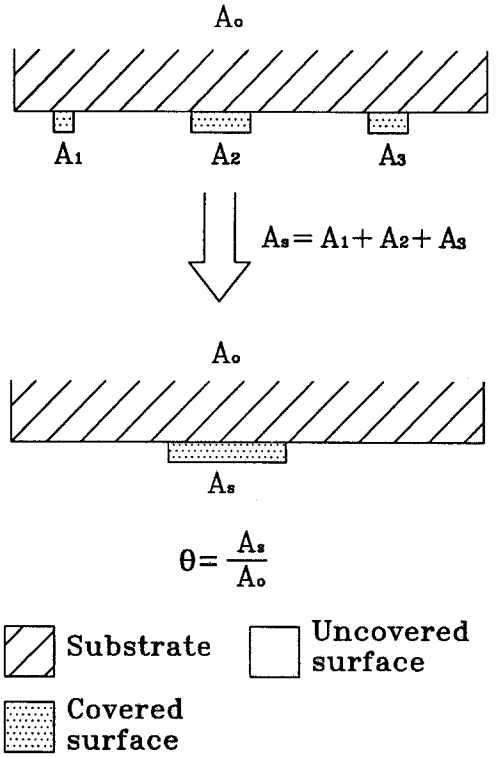

Fig. 7. Schematic definition of surface coverage.

where A_i is the surface area covered by calcareous deposits at time interval i. Surface coverage, by definition, increases with time, and equals 0.0 before the formation of the calcareous deposits and equals 1.0 when the surface is totally covered by the calcareous deposits.

The deposit porosity is defined as the ratio of the total open volume inside the deposits ($V_s - V_d$) to the total volume of the porous deposits (V_s)

$$\epsilon_d = \frac{V_s - V_d}{V_s} \qquad [8]$$

where V_d is the volume occupied by the solid deposits. By assuming that the deposit porosity and tortuosity of the porous layer are constant, the deposit porosity also can be expressed in terms of surface area

$$\epsilon_d = \frac{A_s - A_d}{A_s} = \frac{A_p}{A_s} \qquad [9]$$

where A_d is the surface area occupied by solid deposits and A_p is the uncoated surface area inside the deposits. The surface porosity is then defined as the ratio of total bare surface area ($A_o - A_d$) to the total electrode surface area (A_o)

$$\epsilon_s = \frac{A_o - A_d}{A_o} \qquad [10]$$

It is worth noting that the difference between the deposit porosity and the surface porosity is that the former is based on the total surface area covered by porous deposits (A_s) and the latter is based on the total electrode surface area (A_o). The definitions of ϵ_d and ϵ_s are compared schematically in Fig. 8. By making these definitions and assumptions, the current density is expected to approach to a steady state and nonzero value though the surface coverage is approaching 1.0.

Together with the surface coverage, θ, and the solution potential, Φ, the concentrations of nine components in seawater will be accounted for in the model. The 11 unknowns are numbered in the following way for notational convenience: 1, O_2; 2, H_2; 3, OH^-; 4, Mg^{2+}; 5, Ca^{2+}; 6, CO_3^{2-}; 7, HCO_3^-; 8, Na^+; 9, Cl^-; 10, θ; and 11, Φ.

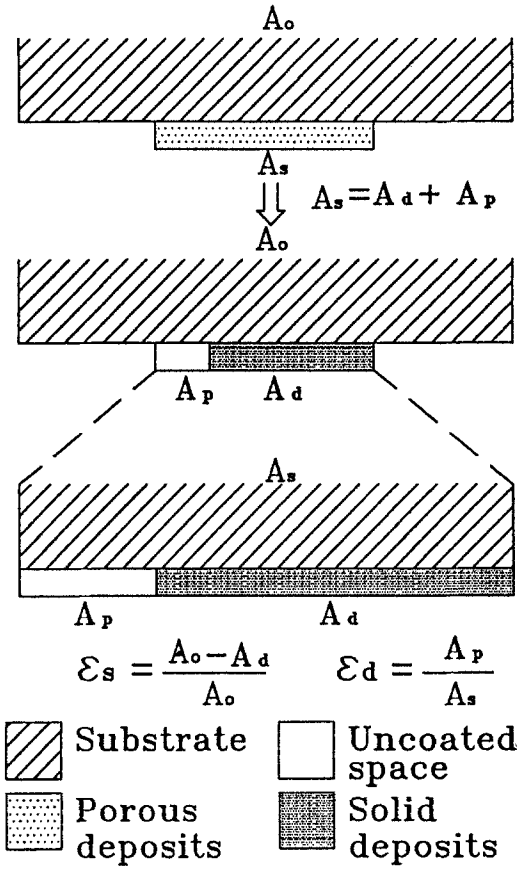

Fig. 8. Schematic definitions of deposit porosity and surface porosity.

Governing equations in the diffusion layer ($0 < y < \delta_{RE}$).— The development of the model starts by considering the material balance of species i in the diffusion layer[20]

$$\frac{\partial c_i}{\partial t} = -\nabla \cdot N_i + R_i \qquad [11]$$

In the solution region, the molar flux expression for species i in y direction depends on migration, diffusion, and convection[20-23]

$$N_i = -\frac{z_i D_i F c_i}{RT}\frac{\partial \Phi}{\partial y} - D_i \frac{\partial c_i}{\partial y} + v_y c_i \qquad i = 1 - 9 \qquad [12]$$

The velocity in the solution is based on the hydrodynamics of the rotating disk[20,22,23]

$$v_y = -a'\Omega\sqrt{\frac{\Omega}{\nu}}y^2 \qquad [13]$$

The only homogeneous reaction in solution is the rapid equilibrium between OH^-, HCO_3^-, and CO_3^{2-} [19] and it is governed by Eq. 14

$$K_{eq} = \frac{c_{CO_3^{2-}}}{c_{OH^-} c_{HCO_3^-}} \qquad [14]$$

Equation 14 is the governing equation for HCO_3^-.

From Eq. 5, it is found that $R_{CO_3^{2-}} = -R_{HCO_3^-}$. Consequently, combining Eq. 11 for $i = 6$ and 7, yields the governing equation for CO_3^{2-} [21]

$$\frac{\partial c_{CO_3^{2-}}}{\partial t} + \frac{\partial c_{HCO_3^-}}{\partial t} = -(\nabla \cdot N_{CO_3^{2-}} + \nabla \cdot N_{HCO_3^-}) \qquad [15]$$

Similarly, $R_{OH^-} = -R_{CO_3^{2-}}$, thus the governing equation for OH^- can be written as

$$\frac{\partial c_{CO_3^{2-}}}{\partial t} + \frac{\partial c_{OH^-}}{\partial t} = -(\nabla \cdot N_{CO_3^{2-}} + \nabla \cdot N_{OH^-}) \qquad [16]$$

Because there is no homogeneous reaction in the solution for species i = 1, 2, 4, 5, 8, and 9, the governing equation becomes

$$\frac{\partial c_i}{\partial t} = -\nabla \cdot N_i \qquad i = 1, 2, 4, 5, 8, 9 \qquad [17]$$

Since the surface coverage is independent of position, its derivative is set to zero everywhere in the solution

$$\frac{\partial \theta}{\partial y} = 0 \qquad [18]$$

By assuming that the solution is electrically neutral, the governing equation for the Φ is

$$\sum_{i=1}^{9} c_i z_i = 0 \qquad [19]$$

Equations 18 and 19 will be the governing equations for θ and Φ in the diffusion layer.

Boundary conditions on the electrode surface ($y = 0$).— Instead of considering the actual geometric detail of porous structures, two parameters, MacMullin number $N_{M,PE}$ for porous layers and deposit porosity ϵ_d, are used to define the average quantities for characterizing the transfer phenomena in the porous layer.[22] The MacMullin number is defined as

$$N_{M,PE} = \frac{\tau}{\epsilon_d} \qquad [20]$$

where τ represents the tortuosity of the porous layer and is set to 1 automatically because the deposit thickness is ignored in the modeled region. The surface porosity ϵ_s is then defined as the summation of the open space in the uncovered surface and the open space inside the covered surface

$$\epsilon_s = (1 - \theta) + \epsilon_d \theta \qquad [21]$$

In essence, Eq. 21 is identical to Eq. 10.

With the assumption that there is no convective flow on the electrode surface and that the deposits are porous, the molar flux for species i becomes

$$N_i = -\frac{z_i D_{i,e} F c_i}{RT}\frac{\partial \Phi}{\partial y} - D_{i,e}\frac{\partial c_i}{\partial y} \qquad i = 1 - 9 \qquad [22]$$

where $D_{i,e}$ is the effective diffusion coefficient in the porous layer and is calculated by the following equation

$$D_{i,e} = D_i(1 - \theta) + \frac{D_i}{N_{M,PE}}\theta \qquad i = 1 - 9 \qquad [23]$$

On the electrode surface, the boundary condition for species i is formulated based on the assumption that the molar flux of species i is equal to the reaction rates of electrochemical and precipitation reactions occurring on the electrode surface

$$N_i = R_i' + R_i'' \qquad [24]$$

Thus, the boundary condition for OH^- is

$$N_{OH^-} = R'_{OH^-} + R''_{OH^-} \qquad [25]$$

Since there is no precipitation reaction for O_2 and H_2, Eq. 24 for i = 1 and 2 can be simplified to

$$N_i = R_i' \qquad i = 1, 2 \qquad [26]$$

By assuming that there is no electrochemical reaction, the boundary condition for Mg^{2+}, Ca^{2+}, and CO_3^{2-} on the electrode surface is

$$N_i = R_i'' \qquad i = 4 - 6 \qquad [27]$$

Because HCO_3^-, Na^+, and Cl^- are involved in neither any electrochemical reactions nor any precipitation reactions on the electrode surface, the molar flux of each of these species is zero

$$N_i = 0 \qquad i = 7 - 9 \qquad [28]$$

By assuming that the deposits are porous and their porosity and thickness are constant, the change in surface coverage with time can be represented by

$$\frac{\partial\theta}{\partial t} = -\frac{1}{(1-\epsilon_d)\delta}\left(\frac{R''_{Ca^{2+}}MW_{CaCO_3}}{\rho_{CaCO_3}} + \frac{R''_{Mg^{2+}}MW_{Mg(OH)_2}}{\rho_{Mg(OH)_2}}\right) \quad [29]$$

The calcareous deposits are assumed to be a mixture of $CaCO_3$ and $Mg(OH)_2$. Equation 29 then will be the boundary condition for θ. Also, the electroneutrality holds on the electrode surface and Eq. 19 is the governing equation of Φ.

The production rate of species i due to the electrochemical reactions[22] is given by Eq. 30

$$R'_i = -\sum_{j=1}^{NR}\frac{s_{ij}i_j}{n_jF} \qquad i = 1-3 \quad [30]$$

where the current density due to electrochemical reaction j is corrected to account for the decrease in active surface area by the following equation

$$i_j = \epsilon_s j_j \quad [31]$$

The local current density j_j generated by electrochemical reaction j is assumed to be described by a Butler-Volmer equation[23-25]

$$j_j = i_{oj,ref}\left\{\prod_i\left(\frac{c_{i,o}}{c_{i,ref}}\right)^{p_{ij}}\exp\left[\frac{\alpha_{aj}F}{RT}\eta_j\right] - \prod_i\left(\frac{c_{i,o}}{c_{i,ref}}\right)^{q_{ij}}\exp\left[\frac{-\alpha_{cj}F}{RT}\eta_j\right]\right\} \quad [32]$$

where

$$i_{oj,ref} = \prod_i i_{oj,data}\left(\frac{c_{i,ref}}{c_{i,data}}\right)^{\gamma_{ij}} \quad [33]$$

and

$$U_{j,ref} = \left[U_j^\theta - \frac{RT}{n_jF}\sum_i s_{ij}\ln\left(\frac{c_{i,ref}}{\rho_o}\right)\right] - U_{RE} \quad [34]$$

The overpotential for electrochemical reaction j, η_j in Eq. 32, is given by

$$\eta_j = V - \Phi_o - U_{j,ref} \quad [35]$$

The reaction order constants $p_{i,j}$ and $q_{i,j}$ are related to $s_{i,j}$ by

$$p_{ij} = s_{ij} \quad q_{ij} = 0 \quad \text{if} \quad s_{ij} > 0$$
$$p_{ij} = 0 \quad q_{ij} = -s_{ij} \quad \text{if} \quad s_{ij} < 0 \quad [36]$$

Also, $\gamma_{i,j}$ is assumed to be related to $s_{i,j}$ in the following way

$$\gamma_{ij} = p_{ij} - \frac{\alpha_{aj}s_{ij}}{n_j} \quad [37]$$

and

$$\gamma_{ij} = q_{ij} + \frac{\alpha_{cj}s_{ij}}{n_j} \quad [38]$$

Previous work[4] showed the $CaCO_3$ phase precipitating from seawater is aragonite rather than calcite, whose nucleation and growth are strongly retarded by the existence of Mg^{2+} ions[26,27] although its solubility is smaller than that of aragonite. The kinetic expression for the growth of aragonite[28] is

$$r_{CaCO_3} = k_{CaCO_3}(S_{CaCO_3} - 1)^m$$
$$= 0 \quad \text{if } S_{CaCO_3} < 1 \quad [39]$$

where k_{CaCO_3} is the rate constant, S_{CaCO_3} is the supersaturation, and m is the reaction order. The supersaturation of $CaCO_3$ is defined as

$$S_{CaCO_3} = \frac{c_{Ca^{2+}}c_{CO_3^{2-}}}{K_{SP,CaCO_3}} \quad [40]$$

where $K_{SP,CaCO_3}$ is the apparent solubility product constant for $CaCO_3$.

For the precipitation of $Mg(OH)_2$, the rate equation will have the form[19]

$$r_{Mg(OH)_2} = k_{Mg(OH)_2}(c_{Mg^{2+}}c^2_{OH^-} - K_{sp,Mg(OH)_2})$$
$$= 0 \quad \text{if} \quad c_{Mg^{2+}}c^2_{OH^-} < K_{sp,Mg(OH)_2} \quad [41]$$

where $K_{SP,Mg(OH)_2}$ is the apparent solubility product constant for $Mg(OH)_2$.

It is assumed that the precipitation reactions occur on the uncovered surface only. The production rate of species i due to the precipitation reaction[22] is given by Eq. 42

$$R''_i = (1-\theta)\sum_{j=1}^{NP}x_{ij}r_j \qquad i = 3-6 \quad [42]$$

where $x_{i,j}$ is the stoichiometric coefficient of species i in the precipitation reaction j. Thus, the precipitation rates of Ca^{2+} and CO_3^{2-} can be calculated by

$$R''_{Ca^{2+}} = -(1-\theta)r_{CaCO_3} \quad [4]$$

and

$$R''_{CO_3^{2-}} = R''_{Ca^{2+}} \quad [44]$$

Similarly, the precipitation rates of Mg^{2+} and OH^- can be calculated by

$$R''_{Mg^{2+}} = -(1-\theta)r_{Mg(OH)_2} \quad [45]$$

and

$$R''_{OH^-} = 2R''_{Mg^{2+}} \quad [46]$$

Boundary conditions at $y = y_{RE}$.—The concentration for each component at $y = y_{RE}$ where the reference electrode is placed is equal to its bulk concentration

$$c_i(y_{RE}, t) = c_{i,bulk} \qquad i = 1-9 \quad [47]$$

At $y = y_{RE}$, the electroneutrality holds and the solution potential is set at a fixed value

$$\Phi(y_{RE}, t) = \Phi_{RE} \quad [48]$$

The derivative of surface coverage is set to zero at the boundary

$$\frac{\partial\theta(y_{RE}, t)}{\partial y} = 0 \quad [49]$$

Initial conditions at $t = 0$.—The initial concentration for each species is equal to its bulk concentration

$$c_i(y, 0) = c_{i,bulk} \qquad i = 1-9 \quad [50]$$

Also, there is no deposit before the application of cathodic protection

$$\theta(y, 0) = 0 \quad [51]$$

Solution Technique

The model equations will be cast in finite difference form and solved using Newman's BAND(J) subroutine[29] with an implicit time-stepping technique to obtain the surface coverage of the calcareous deposits, the concentrations and potential distributions throughout the diffusion layer. The structure of the model equations is listed in Table I.

Once these values are known, the current density due to the individual electrochemical reaction j can be determined using the Butler-Volmer equation, Eq. 32, and adjusted using Eq. 31. Moreover, the total current density can be found by summing the individual current densities[22]

$$i_T = \sum_{j=1}^{NR} i_j \quad [52]$$

Table I. Structure of equations in the model.

Unknown	Governing equation	Boundary conditions at $y = 0$	Boundary conditions at $y = y_{RE}$	Initial condition
c_{O_2}	Eq. 17	Eq. 26	Eq. 47	Eq. 50
c_{H_2}	Eq. 17	Eq. 26	Eq. 47	Eq. 50
c_{OH^-}	Eq. 16	Eq. 25	Eq. 47	Eq. 50
$c_{Mg^{2+}}$	Eq. 17	Eq. 27	Eq. 47	Eq. 50
$c_{Ca^{2+}}$	Eq. 17	Eq. 27	Eq. 47	Eq. 50
$c_{CO_3^{2-}}$	Eq. 15	Eq. 27	Eq. 47	Eq. 50
$c_{HCO_3^-}$	Eq. 14	Eq. 28	Eq. 47	Eq. 50
c_{Na^+}	Eq. 17	Eq. 28	Eq. 47	Eq. 50
c_{Cl^-}	Eq. 17	Eq. 28	Eq. 47	Eq. 50
θ	Eq. 18	Eq. 29	Eq. 49	Eq. 51
Φ	Eq. 19	Eq. 19	Eq. 48	—

Also, the molar ratio of the $CaCO_3$ to $Mg(OH)_2$ in the deposits at time t can be computed in a straightforward way

$$x_{Ca^{2+}/Mg^{2+},t} = \frac{\sum_t R_{Ca^{2+},t}}{\sum_t R_{Mg^{2+},t}} \quad [53]$$

and similarly the $Mg(OH)_2$ to $CaCO_3$

$$x_{Mg^{2+}/Ca^{2+},t} = \frac{\sum_t R_{Mg^{2+},t}}{\sum_t R_{Ca^{2+},t}} \quad [54]$$

Parameters

The parameters used in the model are listed in Tables II-VI. All of the parameters are reported at 25°C and 35 ppt salinity or have been adjusted to 25°C and 35 ppt salinity. An example using the parameters in Tables II-VI was studied and is discussed in the next section.

Results and Discussion

Concentration profiles.—The concentration profiles of some components in seawater are revealed in Fig. 9-12. The transport of dissolved O_2 is limited, and its concentration was near zero on the electrode surface as shown in Fig. 9. This indicates that the oxygen reduction rate is controlled by mass transfer of oxygen from the bulk solution to the electrode surface. Figure 10 implies a steep gradient of pH in the diffusion layer due to the production of OH^- ions on the electrode surface. Because of the buffering effect in the homogeneous reaction, the solution does not become very alkaline except at the region close to the electrode surface.

Table II. Fixed physical parameters in the model.

Parameter	Value
T	298.15 K
Ω	50 rpm
ρ_o	1.0234×10^{-3} [a] Kg/cm^3
ν	9.33×10^{-2} [a] cm^2/s
τ	1.0
ϵ_d	0.25[b]
y_{RE}	1.5×10^{-2} [c] cm
δ	1.0×10^{-3} [d] cm
V	0.0[e] V
Φ_{RE}	0.9[e] V
U_{RE}	0.242[f] V

[a] Taken from Ref. 32.
[b] The residual current density is about 25% of the current density at 0.5 h.
[c] Calculated from the equation in Ref. 33 and multiplied by 1.5.
[d] Observed from the deposit morphology in Fig. 5.
[e] Chosen arbitrarily to set $V - \Phi_{RE} = -0.9$ V(SCE).
[f] Taken from Ref. 20.

Table III. Kinetic and thermodynamic parameters for the electrochemical reactions in the model.

Reaction	α_{aj}	α_{cj}	n_j	$i_{oj,data}$ (A/cm^2)	U_j^θ (V)
$O_2 + 2H_2O + 4e^- \rightleftarrows 4OH^-$	1	1	2	1.24×10^{-24} [a]	0.401[b]
$2H_2O + 2e^- \rightleftarrows 2OH^- + H_2$	3	1	4	2.0×10^{-11} [c]	−0.828[b]

For oxygen reduction, $c_{O_2,data} = 1.0 \times 10^{-7}$ [a] mol/cm^3, $c_{OH^-,data} = 1.0 \times 10^{-10}$ [a] mol/cm^3.
For hydrogen evolution, $c_{H_2,data} = 6.7 \times 10^{-10}$ [c] mol/cm^3, $c_{OH^-,data} = 1.6 \times 10^{-9}$ [c] mol/cm^3.
[a] Taken from Ref. 22.
[b] Taken from Ref. 20.
[c] Chosen arbitrarily.

Table IV. Parameters of reaction constants and apparent solubility product constants of the precipitation reactions in the model.

Reaction	K_{sp}	k	m
1	6.96×10^{-13} [a] mol^2/cm^6	1.13×10^{-12} [b] mol/cm$^2 \cdot$ s	1.7[b]
2	4.50×10^{-19} [c] mol^3/cm^9	3.7×10^{7} [d] cm^7/mol$^2 \cdot$ s	—

Reaction 1: $Ca^{2+} + CO_3^{2-} \rightarrow CaCO_3$.
Reaction 2: $Mg^{2+} + 2OH^- \rightarrow Mg(OH)_2$.
[a] Taken from Ref. 34.
[b] Taken from Ref. 16.
[c] Taken from Ref. 4.
[d] Taken from Ref. 19 and adjusted to 25°C.

Table V. Parameters of the homogeneous reaction in the model.

Reaction	K_{eq}
$HCO_3^- + OH^- \rightleftarrows CO_3^{2-} + H_2O$	8.40×10^{7} [a] cm^3/mol

[a] Predicted from the equations in Ref. 35.

Table VI. Diffusion coefficients and concentrations of the components in seawater in the model.

Species	D_i (cm^2/s) $\times 10^5$	$C_{i,ref}$ (mol/cm^3)
O_2	2.90[a]	2.11×10^{-8} [b]
H_2	6.28[c]	6.7×10^{-11} [b]
OH^-	5.27[d]	1.6×10^{-9} [e]
Mg^{2+}	0.705[d]	5.45×10^{-5} [f]
Ca^{2+}	0.793[d]	1.05×10^{-5} [f]
CO_3^{2-}	0.955[d]	2.07×10^{-7} [e]
HCO_3^-	1.19[d]	1.54×10^{-6} [e]
Na^+	1.34[d]	4.30×10^{-4} [g]
Cl^-	2.03[d]	5.58×10^{-4} [f]

[a] Chosen arbitrarily.
[b] Predicted from the equations in Ref. 32.
[c] Taken from Ref. 19 and ajdusted to 25°C.
[d] Taken from Ref. 36.
[e] Predicted from the equations in Ref. 35.
[f] Taken from Ref. 35.
[g] Taken from Ref. 35 and adjusted to meet the electroneutrality.

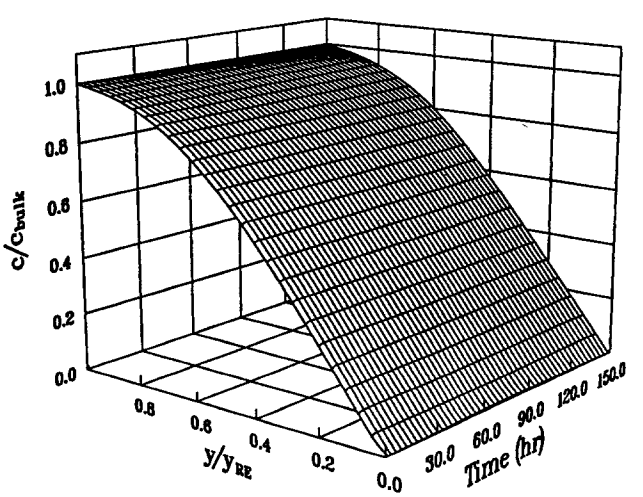

Fig. 9. Dimensionless concentration profile of O_2 inside the diffusion layer ($y_{RE} = 1.5 \times 10^{-2}$ cm, $c_{O_2,bulk} = 2.1 \times 10^{-7}$ mol/cm^3).

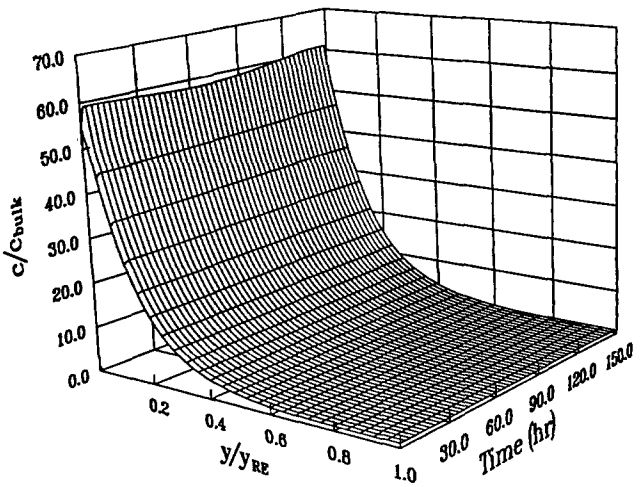

Fig. 10. Dimensionless concentration profile of OH^- ions inside the diffusion layer ($y_{RE} = 1.5 \times 10^{-2}$ cm, $c_{OH^-,bulk} = 1.6 \times 10^{-9}$ mol/cm^3).

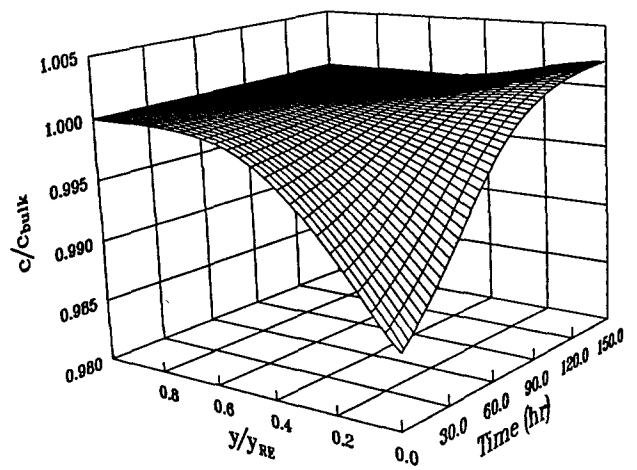

Fig. 11. Dimensionless concentration profile of Ca^{2+} ions inside the diffusion layer ($y_{RE} = 1.5 \times 10^{-2}$ cm, $c_{Ca^{2+},bulk} = 1.1 \times 10^{-5}$ mol/cm^3).

Figure 11 shows that the concentration of Ca^{2+} ions does not change much inside the diffusion layer. While, Fig. 12 shows that the concentration of CO_3^{2-} ions increases about eight times on the electrode surface due to the homogeneous reaction. Thus, the supersaturation of $CaCO_3$ is controlled by the concentration of CO_3^{2-} ions, and the higher concentration of CO_3^{2-} ions on the electrode surface is the driving force for the formation of $CaCO_3$.

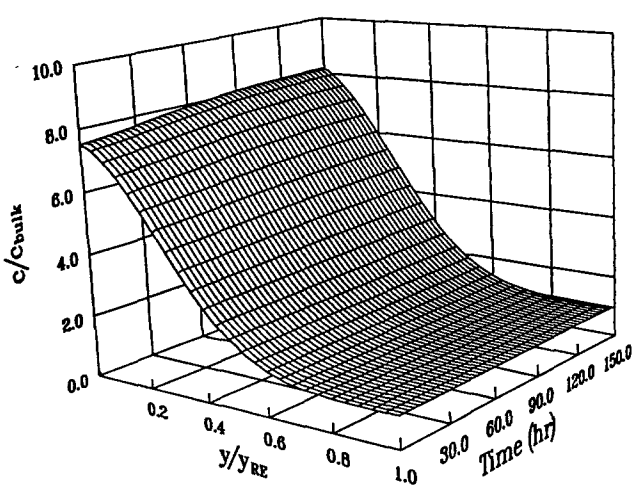

Fig. 12. Dimensionless concentration profile of CO_3^{2-} ions inside the diffusion layer ($y_{RE} = 1.5 \times 10^{-2}$ cm, $c_{CO_3^{2-},bulk} = 1.8 \times 10^{-7}$ mol/cm^3).

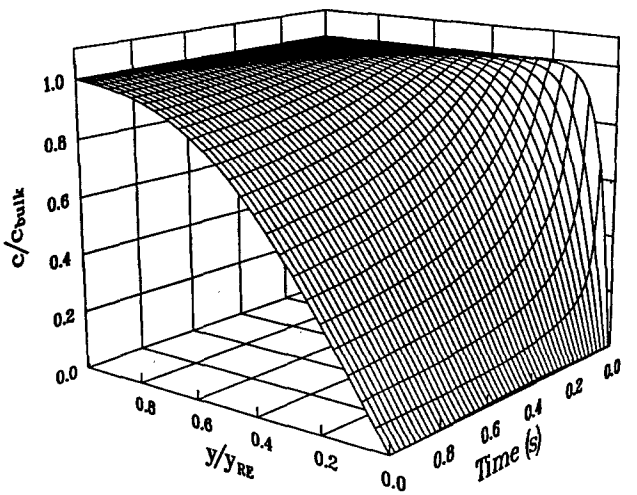

Fig. 13. Dimensionless concentration profile of O_2 inside the diffusion layer during the initial stage ($y_{RE} = 1.5 \times 10^{-2}$ cm, $c_{O_2,bulk} = 2.1 \times 10^{-7}$ mol/cm^3).

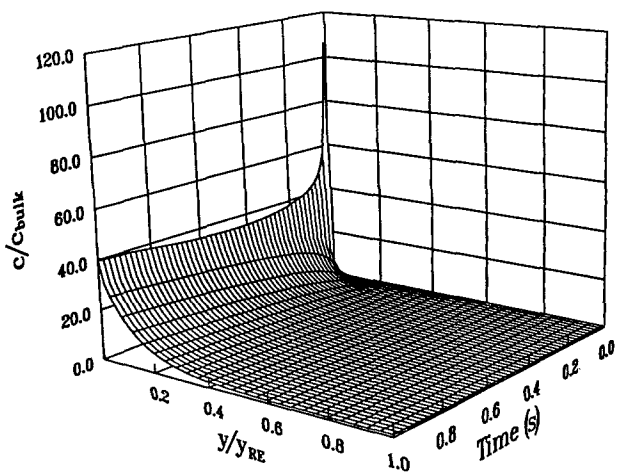

Fig. 14. Dimensionless concentration profile of OH^- ions inside the diffusion layer during the initial stage ($y_{RE} = 1.5 \times 10^{-2}$ cm, $c_{OH^-,bulk} = 1.6 \times 10^{-9}$ mol/cm^3).

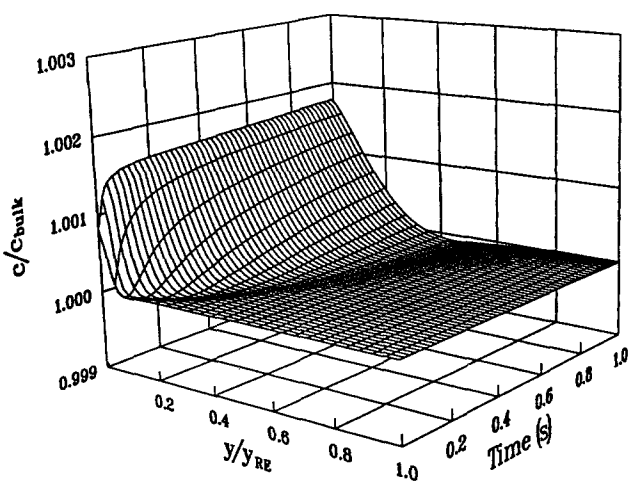

Fig. 15. Dimensionless concentration profile of Mg^{2+} ions inside the diffusion layer during the initial stage ($y_{RE} = 1.5 \times 10^{-2}$ cm, $c_{Mg^{2+},bulk} = 5.5 \times 10^{-5}$ mol/cm^3).

Figures 13-15 show the concentration profiles of some components in seawater in the diffusion layer within 1 s. The rapid drop in oxygen concentration, as shown in Fig. 13, indicates that oxygen is depleted after 1 s. As a result, the concentration of OH^- ions also drops very

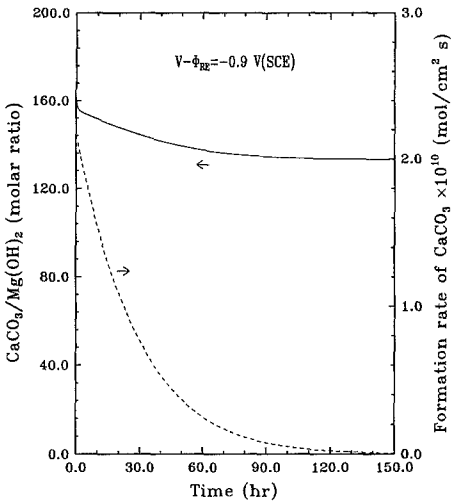

Fig. 16. Change of the molar ratio of $CaCO_3$ to $Mg(OH)_2$ in the deposits on cathodically protected steel in seawater with time.

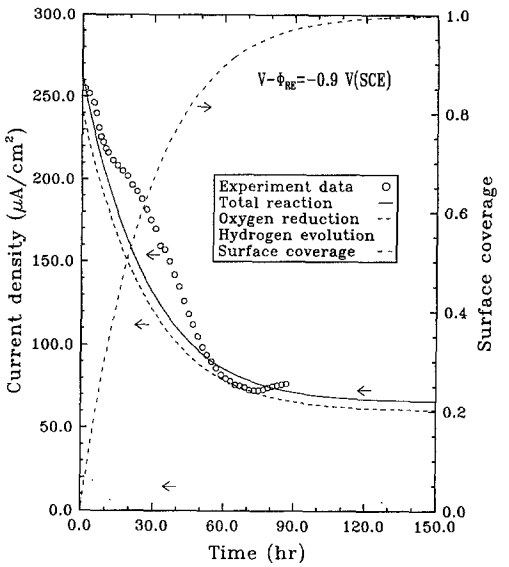

Fig. 18. Changes of current density and surface coverage on cathodically protected steel in seawater with time.

quickly as shown in Fig. 14. Figure 15 implies that Mg^{2+} ions are not depleted on the electrode surface. Therefore, the formation of $Mg(OH)_2$ is totally governed by the concentration of OH^- ions.

Composition of calcareous deposits.—Although the formation of $Mg(OH)_2$ is favorable kinetically, the supersaturation of $Mg(OH)_2$ is much lower than that of $CaCO_3$. Consequently, $CaCO_3$ forms much faster than $Mg(OH)_2$ and the deposits contain mostly $CaCO_3$ as shown in Fig. 16.

$Mg(OH)_2$ is highly soluble in seawater and its precipitation is controlled by the concentration of OH^- ions, which are produced substantially only when the concentration of dissolved O_2 on the electrode surface is highest. Therefore, the initial deposits are expected to contain more $Mg(OH)_2$ than $CaCO_3$ as shown in Fig. 17.

Current density and surface coverage.—Figure 18 shows the changes of current density and surface coverage with time from the results of the model. The current density was found to drop very quickly and continued to decrease with time but at much slower rates. After the electrode surface was almost covered, the current density became nearly constant. However, the residual current density was never equal to zero due to the porous nature of the calcareous deposits. Therefore, the calcareous deposits could be viewed as a porous film with fixed thickness and porosity once the formation is complete.

According to the Butler-Volmer equation in Eq. [32], the current density for an electrochemical reaction depends on the concentrations of the reacting species and the overpotential on the electrode surface. In the present model, the superficial current density was corrected to account for the inactive surface area occupied by the calcareous deposits as described in Eq. 31. Results from the concentration profiles reveal that the concentrations of the reacting species and the overpotential on the electrode surface are nearly steady with time. Therefore, the increase of surface coverage with time in Fig. 18 indicates that the main reason for the drop of current density is the formation of calcareous deposits. The calcareous deposits on the electrode surface reduce the active surface area available for the electrochemical reactions. This results in the decrease of the cathodic current density.

The comparison on the current density between the experimental data and the results predicted from the model is shown in Fig. 18. From the results of the experiment, it is found that the current density did not change much during the first few hours of exposure. This probably results from the retarded nucleation for $CaCO_3$ crystals[26,27] on the electrode surface, which is ignored in the model. Moreover, the current density in the middle of the experiment did not decrease as fast as the model predicts. This might be due to the removal of deposits and the loss of adhesion of deposits from the electrode surface.[30] To improve the present model, the processes of nucleation and dissolution of deposits should be taken into consideration.

Figure 18 also shows the changes in the partial current densities for oxygen reduction and hydrogen evolution under CP. It is believed that calcareous deposits are capable of decreasing the rate of oxygen reduction reaction by functioning as a barrier to oxygen transport; however, their influence on hydrogen evolution is limited apparently because this reaction is activation controlled and does not require mass transport.[31] Our model predictions indicate calcareous deposits not only reduce the transport rate of oxygen to the substrate surface but also reduce the active surface area available for the electrochemical reactions. This results in a decrease in the cathodic current densities for both oxygen reduction and hydrogen evolution.

Figure 19 shows the quick drop of the total current density and the partial current density for the oxygen reduction due to oxygen depletion on the electrode surface. It is found from Fig. 19 that the concentration of O_2 drops very quickly during the initial stage. However, the change of the partial current density for hydrogen evolution is relatively

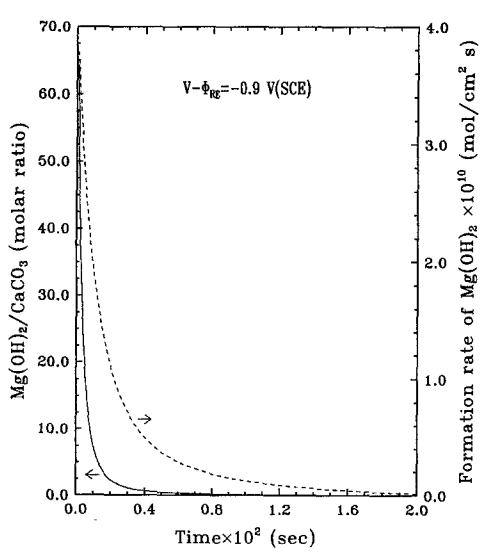

Fig. 17. Change of the molar ratio of $Mg(OH)_2$ to $CaCO_3$ in the deposits on cathodically protected steel in seawater during the initial stage.

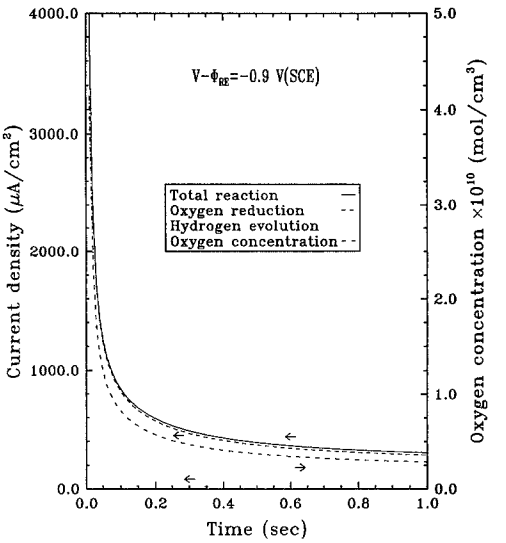

Fig. 19. Current density decay and surface oxygen depletion on cathodically protected steel in seawater during the initial stage.

unchanged. Apparently, the main drop in the total current density results from the decreasing rate of the oxygen reduction. Therefore, it is reasonable to point out that the sharp drop of current density during the initial stage is attributed to the oxygen depletion on the electrode surface.

Conclusions

From the results and discussion, the following conclusions are presented:

1. The increase in the concentration of OH^- ions on the electrode surface is the main driving force for the formation of calcareous deposits.
2. The calcareous deposits contain mostly $CaCO_3$ while the initial deposits are expected to contain more $Mg(OH)_2$ than $CaCO_3$.
3. There are two stages that occur during the drop of current density under CP. The first almost instantaneous drop (within a second) in the current density is attributed to the oxygen depletion on the electrode surface, and the second decrease of the current density is associated with the formation of the calcareous deposits on the electrode surface.
4. The calcareous deposits on the electrode surface reduce the active surface area available for the electrochemicial reactions. This results in a decrease in the cathodic current density.

Acknowledgments

The authors are grateful for the financial support of this work by Offshore Technology Research Center (OTRC) at Texas A&M University.

Manuscript submitted April 27, 1992; revised manuscript Nov. 12, 1992.

Texas A&M University assisted in meeting the publication costs of this article.

LIST OF SYMBOLS

a'	disk hydrodynamic constant, 0.51023
A_o	total electrode surface area, cm^2
A_d	surface area occupied by solid deposits inside the deposits, cm^2
A_i	surface area occupied by porous deposits at time interval i, cm^2
A_p	uncoated surface area inside the deposits, cm^2
A_s	surface area occupied by porous deposits on the electrode surface, cm^2
c_i	concentration of species i, mol/cm^3
$c_{i,bulk}$	bulk solution concentration of species i, mol/cm^3
$c_{i,data}$	data solution concentration of species i, mol/cm^3
$c_{i,o}$	concentration of species i on the electrode surface, mol/cm^3
$c_{i,ref}$	reference concentration of species i, mol/cm^3
D_i	diffusion coefficient of species i, cm^2/s
$D_{i,e}$	effective diffusion coefficient of species i in the porous layer, cm^2/s
F	Faraday's constant, 96487 C/mol
i_j	superficial current density for electrochemical reaction j, A/cm^2
i_T	total current density, A/cm^2
j_j	local current density for electrochemical reaction j, A/cm^2
k_{CaCO_3}	reaction rate constant for the precipitation reaction of $CaCO_3$, mol/cm^2 · s
$k_{Mg(OH)_2}$	reaction rate constant for the precipitation reaction of $Mg(OH)_2$, cm^7/mol^2 · s
K_{eq}	equilibrium constant for the homogeneous reaction, cm^3/mol
$K_{sp,CaCO_3}$	apparent solubility product constant of $CaCO_3$, mol^2/cm^6
$K_{sp,Mg(OH)_2}$	apparent solubility product constant of $Mg(OH)_2$, mol^3/cm^9
m	reaction order for the precipitation of $CaCO_3$
MW_{CaCO_3}	molecular weight of $CaCO_3$, g/mol
$MW_{Mg(OH)_2}$	molecular weight of $Mg(OH)_2$, g/mol
n_j	number of electrons transferred in electrochemical reaction j
N_i	molar flux of species i, mol/cm^2 · s
$N_{M,PE}$	MacMullin number for porous layer
NP	number of precipitation reaction
NR	number of electrochemical reaction
p_{ij}	anodic reaction order of species i in electrochemical reaction j
q_{ij}	cathodic reaction order of species i in electrochemical reaction j
r_j	precipitation rate of j deposit, mol/cm^2 · s
R	universal gas constant, 8.314 J/mol · K
R_i	homogeneous reaction rate of species i, mol/cm^2 · s
R_i'	electrochemical reaction rate of species i, mol/cm^2 · s
R_i''	precipitation rate of species i, mol/cm^2 · s
s_{ij}	stoichiometric coefficient of species i in the electrochemical reaction j
S_{CaCO_3}	supersaturation for $CaCO_3$
t	time, s
T	temperature, K
$U_{j,ref}$	equilibrium potential for electrochemical reaction j at reference concentration of species i, V
U_j^θ	standard electrode potential for electrochemical reaction j, V
U_{RE}	reference electrode potential at reference concentrations, V
v_y	velocity of solution in y direction, cm/s
V	electrode potential, V
V_d	volume occupied by solid deposits on V_s, cm^3
V_s	volume occupied by porous deposits on V_o, cm^3
$x_{Ca^{2+}/Mg^{2+},t}$	molar ration of $CaCO_3$ to $Mg(OH)_2$ in the deposits at time t
$x_{Mg^{2+}/Ca^{2+},t}$	molar ration of $Mg(OH)_2$ to $CaCO_3$ in the deposits at time t
x_{ij}	stoichiometric coefficient of species i in the precipitation reaction j
y	normal coordinate in modeled region, cm
y_{RE}	position of reference electrode, cm
z_i	charge number of species i

Greek

α_{aj}	anodic transfer coefficient for reaction j
α_{cj}	cathodic transfer coefficient for reaction j
γ_{ij}	exponent in the composition dependent of the exchange current density for species i in electrochemical reaction j
δ	thickness of calcareous deposits, cm
ϵ_d	deposit porosity
ϵ_s	surface porosity
η_j	overpotential, V
ν	kinematic viscosity, cm^2/s
Ω	disk rotation velocity, s^{-1}
Φ	solution potential, V
Φ_o	solution potential on the electrode surface, V
Φ_{RE}	solution potential in bulk solution, V
ρ_{CaCO_3}	density of $CaCO_3$, g/cm^3
$\rho_{Mg(OH)_2}$	density of $Mg(OH)_2$, g/cm^3

τ tortuosity of porous layer
θ surface coverage of calcareous deposits

REFERENCES

1. M. G. Fontana, *Corrosion Engineering,* 3rd ed., McGraw-Hill, Inc., New York (1986).
2. W. H. Hartt, W. Wang, and T. Y. Chen, Paper No. 576, presented at "CORROSION/89," National Association of Corrosion Engineers, Houston, TX (1989).
3. K. P. Fischer and W. H. Thomason, Paper No. 577, presented at "CORROSION/89," National Association of Corrosion Engineers, Houston, TX (1989).
4. W. H. Hartt, C. H. Culberson, and S. W. Smith, *Corrosion,* **40,** 11, 609 (1984).
5. H. A. Humble, *ibid.,* **4,** 7, 358 (1948).
6. H. R. England and R. H. Heidersbach, CH1685-7, IEEE (1981).
7. S. L. Wolfson and W. H. Hartt, *Corrosion,* **37,** 2, 70 (1981).
8. M. M. Kunjapur, W. H. Hartt, and S. W. Smith, *ibid.,* **43,** 11, 674 (1987).
9. J. E. Finnegan and K. P. Fischer, Paper No. 581, presented at "CORROSION/89," National Association of Corrosion Engineers, Houston, TX (1989).
10. K. E. Mantel, W. H. Hartt, and T. Y. Chen, Paper No. 374, presented at "CORROSION/90," National Association of Corrosion Engineers, Houston, TX (1990).
11. J-S. Luo and W. H. Hartt, Paper No. 236, presented at "CORROSION/91," National Association of Corrosion Engineers, Houston, TX (1991).
12. J. S. Luo, R. U. Lee, T. Y. Chen, W. H. Hartt, and S. W. Smith, *Corrosion,* **47,** 3, 189 (1991).
13. S. Elbeik, A. C. C. Tseung, and A. L. Mackay, *Corros. Sci.,* **26,** 669 (1986).
14. S-H. Lin and S. C. Dexter, *Corrosion,* **44,** 9, 615 (1988).
15. G. K. Sadasivan, M. S. Thesis, Florida Atlantic University, Boca Raton, FL (1989).
16. J. Burton, *Chem. Ind.,* **16,** 550 (1977).
17. S. C. Dexter and S-H. Lin, Paper No. 499, presented at "CORROSION/91," National Association of Corrosion Engineers, Houston, TX (1991).
18. American Society of Testing and Materials, Designation D 1141-90, Philadelphia, PA (1990).
19. A. Turnbull and D. H. Ferriss, *Corros. Sci.,* **26,** 601 (1986).
20. J. S. Newman, *Electrochemical Systems,* Prentice-Hall, Inc., Englewood Cliffs, NJ (1973).
21. P. Russell and J. Newman, *This Journal,* **133,** 59 (1986).
22. W. E. Ryan, R. E. White, and S. L. Kelly, *ibid.,* **134,** 2154 (1987).
23. K-M Yin and R. E. White, *AIChE J.,* 36, 187 (1990).
24. H. Gu, T. V. Nguyen, and R. E. White, *This Journal,* **134,** 2953 (1987).
25. T. Yeu, T. V. Nguyen, and R. E. White, *ibid.,* **135,** 1971 (1988).
26. R. M. Pytkowicz, *Am. J. Sci.,* **273,** 515 (1973).
27. R. A. Berner, *Geochim. Cosmochim. Acta,* **39,** 489 (1975).
28. E. A. Burton and L. M. Walter, *Geology,* **15,** 111 (1987).
29. J. S. Newman, *Ind. Eng. Chem. Fundam.,* **7,** 514 (1968).
30. K. P. Fischer and J. E. Finnegan, Paper No. 582, presented at "CORROSION/89," National Association of Corrosion Engineers, Houston, TX (1989).
31. R. U. Lee and J. R. Ambrose, *Corrosion,* **44,** 12, 887 (1988).
32. M. Whitfield and D. Janger, *Marine Electrochemistry,* John Wiley & Sons, Inc., New York (1981).
33. A. J. Bard and L. R. Faulkner, *Electrochemical Methods,* John Wiley & Sons, Inc., New York (1980).
34. A. Mucci, *Am. J. Sci.,* **283,** 780 (1983).
35. G. Skirrow, in *Chemical Oceanography,* Vol. 2, 2nd ed., J. P. Riley and G. Skirrow, Editors, Academic Press, Inc., New York (1975).
36. Y.-H. Li and S. Gregary, *Geochim. et Cosmochim. Acta,* **38,** 703 (1974).

Electrochemical Oxidation of Graphite in Organic Electrolytes Containing PF_6^- or ClO_4^-

Zhengwei Zhang* and Michael M. Lerner**

Department of Chemistry and Center for Advanced Materials Research, Oregon State University, Corvallis, Oregon 97331-4003

ABSTRACT

A systematic evaluation of the electrochemical oxidation of porous graphite powder electrodes in CH_3NO_2, CH_3CN, and propylene carbonate (PC) electrolytes containing PF_6^- or ClO_4^- is described. The graphite compounds obtained are characterized by x-ray powder diffraction while in the electrolyte solution and following evacuation. The potential-charge curves reveal a number of common features which are used to estimate the efficiency of the galvanostatic charge process in the different electrolytes. The stabilities of the intercalation compounds are also examined by a recharge method. The CH_3NO_2-based electrolytes with either anion yield charge efficiencies of greater than 90% to a charge input of 4 C/mmole carbon (C_{24}^+), and the oxidized products are stable in the electrolyte solution. The CH_3CN-based electrolytes are far less efficient and the oxidized compounds produced decompose rapidly. Low-stage products can be isolated following oxidation in PC saturated with $NaPF_6$, but not when the 0.5*M* $LiClO_4$, PC electrolyte is employed.

Graphite can be chemically or electrochemically oxidized to form intercalation compounds. The preparation of graphite salts via the chemical route allows for the rapid production of relatively large and homogeneous samples; however, electrochemical syntheses offer other advantages. The oxidation can be controlled and intermediate phases not readily obtained by chemical methods can therefore be isolated. The progress of the electrochemical oxidation may be continuously monitored by potential-charge plots, and, if side reactions are not significant, coulommetry unambiguously provides the charge borne by carbon. The latter point is especially important as the nature of the charge distribution in chemically prepared intercalation compounds has been a source of controversy for some time.[1-3]

The oxidative electrochemistry of graphite is also of practical interest. The charge/discharge cycle associated with graphite intercalation has been suggested as a positive electrode for reversible, high energy density cells.[4,5] The stability of the oxidized products formed is therefore a technologically important issue.

Suitable electrolytes must be stable to the high potentials required to remove electrons from the carbon π-bands. The required electromotive force is a function of the charge on carbon (related to the work function of graphite), which, for highly charged compounds, can exceed +1.5 V *vs.* SHE. Nevertheless, a number of electrolytes have been investigated, including the concentrated aqueous acids H_2SO_4,[6-10]

* Electrochemical Society Student Member.
** Electrochemical Society Active Member.